The steady propagation of a bubble in a flexible-walled channel: Asymptotic and computational models

O. E. Jensen
Division of Applied Mathematics, School of Mathematical Sciences, University of Nottingham, University Park, Nottingham NG7 2RD, United Kingdom

M. K. Horsburgh
Department of Applied Mathematics and Theoretical Physics, University of Cambridge, Silver Street, Cambridge CB3 9EW, United Kingdom

D. Halpern
Department of Mathematics, 345 Gordon Palmer Hall, University of Alabama, Tuscaloosa, Alabama 35487

D. P. Gaver III
Department of Biomedical Engineering, Tulane University, New Orleans, Louisiana 70118-5674

(Received 25 July 2001; accepted 8 November 2001)

The steady motion at zero Reynolds number of a semi-infinite bubble through a fluid-filled, flexible-walled channel, a model for the reopening of a collapsed lung airway, is described using asymptotic and numerical methods. The channel walls are membranes that are supported by external springs and are held under large longitudinal tension. An asymptotic analysis is presented under the assumption that membrane slopes are uniformly small. Near the bubble tip, the flow is equivalent to that of a semi-infinite bubble in a weakly tapered channel. Key features of this two-dimensional flow are matched to long-wavelength approximations describing the remainder of the solution domain. The analysis is valid for a wide range of bubble speeds, and it takes a particularly simple form when the bubble peels apart the channel walls as it advances. Predictions of bubble pressure as a function of bubble speed are validated by comparison with existing computations, new boundary-element simulations describing bubble motion in a channel with one rigid and one deformable wall, and experiments. © *2002 American Institute of Physics.* [DOI: 10.1063/1.1432694]

I. INTRODUCTION

For many viscous flows involving an advancing free boundary, the speed of propagation is set by local conditions at the advancing boundary. Examples include the slow spreading of a viscous drop over a plane when contact-line dynamics are dominant,[1–3] the propagation of fluid-filled cracks,[4,5] and two-phase flow in a confined geometry such as a Hele–Shaw cell.[6,7] Here we consider an example of such a flow that is of fundamental importance in pulmonary mechanics: the reopening by an air bubble of an initially collapsed, fluid-filled lung airway.

For sufferers of asthma, emphysema, cystic fibrosis and infant or adult respiratory distress syndrome (IRDS and ARDS, respectively), it is common for small lung airways to become blocked with fluid as a result of surface-tension-driven instabilities of the airways liquid lining.[8,9] The airway walls may then collapse as a result of low capillary pressures. Physiologically, this condition is extremely significant, as these obstructed airways must be opened to restore adequate gas exchange. Medical treatment of this problem includes the delivery of surfactant for IRDS,[10] which indicates the importance of the liquid-lining surface tension in this disease. Additionally, for those with ARDS, the medical focus centers on strategies that might reduce ventilator-induced lung injury of sensitive airway and alveolar epithelial cells. For example, if ventilator settings are not modified when significant airway closure occurs, hyperinflation of open regions of the lung can lead to stretch-induced injury of healthy alveoli. Much attention has recently been placed on this behavior, because clinical studies have shown that a radical decrease in ventilation tidal volumes can significantly reduce mortality of ARDS.[11] Recent studies also suggest that cellular damage might be caused by repetitive closure and reopening that exerts local stresses on airway and alveolar walls,[12] signifying the importance of fluid–structure interactions on this disease.

The airway reopening process can be partially understood through a model problem in which a two-dimensional bubble penetrates a fluid-filled channel, the walls of which are formed by membranes supported by external springs and held under longitudinal tension (see Fig. 1).[13–16] The combination of springs and tension is used to mimic the primary elastic forces in a three-dimensional airway wall; the springs limit transverse wall displacements where the channel is uniformly inflated, a role played by hoop stresses in a cylindrical airway. The viscous fluid that occludes the channel is assumed to be Newtonian with constant viscosity μ^* and constant surface tension γ^*. Experiments show that the steady-state speed of bubble propagation U^* is an increasing function of the imposed bubble pressure p_b^*, but that a threshold ''yield'' bubble pressure must be exceeded for steady bubble propagation to occur.[15–17] This yield pressure

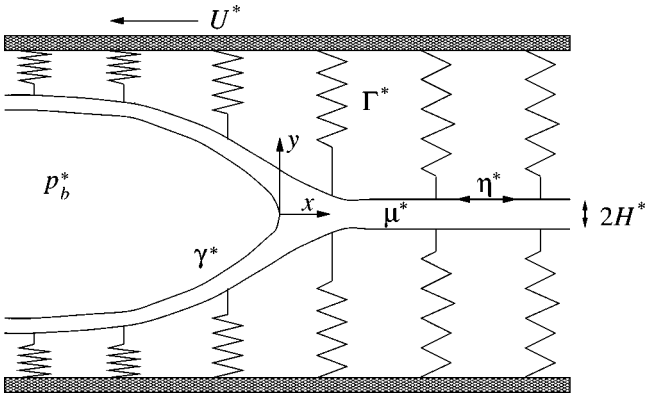

FIG. 1. A semi-infinite bubble at pressure p_b^* advancing at speed U^* into a planar fluid-filled channel, shown in the frame of the bubble tip.

is significant because it determines the pressure necessary to introduce air to obstructed portions of the lung. Theoretical investigations are necessary to help determine whether the reopening process generates stresses that are large enough to result in damage to delicate airway walls.

Numerical solutions of this model problem, obtained using boundary-element[13] and finite-element[14] methods, have identified two steady solution branches (shown schematically in Fig. 2), which originate at a saddle-node bifurcation (taking p_b^* as a control parameter). The left-hand branch in Fig. 2 represents steady solutions for which p_b^* decreases as U^* increases; for these solutions the channel is widely inflated over a long distance ahead of the bubble, and the bubble pushes ahead of itself a long column of fluid. Bretherton's theory[18] for the slow advance of a bubble in a rigid-walled channel was used in Ref. 13 to show that, along the left branch, $p_b^* \propto U^{*-2/3}$, provided the capillary number $\mathrm{Ca} = \mu U^*/\gamma^*$ is sufficiently small. The right-hand branch in Fig. 2 corresponds to solutions for which p_b^* increases with U^*, and for which the walls of the inflated section of channel have a higher taper angle and the bubble is more pointed; this case is suggestive of a 'peeling' motion. The same general behavior is seen at both zero[13] and nonzero[14] Reynolds numbers. Experimental evidence[15–17] suggests that the left branch is unstable to perturbations at constant p_b^*, and the right branch stable.

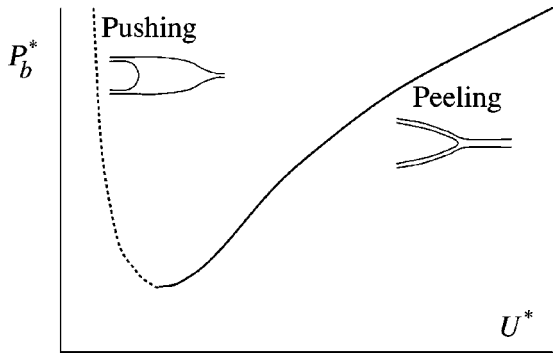

FIG. 2. Steady solutions of the symmetric reopening problem, shown schematically (after Ref. 13). Approximate bubble and membrane shapes are shown for pushing and peeling motions.

In this paper we have two aims. First, we present an asymptotic description of both steady solution branches (identified in Ref. 13) that is not subject to the usual restriction $\mathrm{Ca} \ll 1$. Instead, the analysis developed below relies on the assumption that the membrane tension is large, so that the membrane slope is uniformly small. The asymptotic approximation will be shown to agree well with existing numerical predictions[13] at zero Reynolds number even when $\mathrm{Ca} = O(1)$. Particularly simple predictions of the $p_b^* - U^*$ relationship arise when the channel is widely inflated and the bubble advances with a peeling motion, characteristic of that identified by McEwan and Taylor.[19] Second, since this theoretical model for airway reopening has not hitherto been compared quantitatively to experiment, we compare new computational results and asymptotic predictions against experimental data[16] for a system in which a bubble advances into a channel formed by a rigid wall and a deformable wall, an asymmetric configuration shown in Fig. 9.

The inspiration for the asymptotic analysis comes in part from Ruschak,[20] who showed how roll-coating flows involving a meniscus between two closely spaced cylinders may be treated by combined asymptotic and numerical methods. The key observation, originally due to Taylor,[21] is that the flow may be treated using lubrication theory everywhere except in a neighborhood of the meniscus tip, a region having length comparable to the local gap width, in which the full two-dimensional Stokes equations must be solved. In both Ruschak's problem and the present case, the walls are locally almost parallel in this inner region, which simplifies the calculation, reducing it at leading order to the widely studied ''Bretherton'' problem of a semi-infinite bubble advancing into a parallel-sided fluid-filled channel at zero Reynolds number. A numerical approach to this problem is demanded unless the capillary number is vanishingly small;[6,18] the numerical results of Ruschak[20] and others[22–24] for this inner problem will be exploited here, as will Ruschak's overall asymptotic approach (which has been validated for the roll-coating problem[25]). However, for our asymptotic approximation to be valid to the required order, we must extend Ruschak's approach by accounting explicitly for the leading-order effects of channel taper in the neighborhood of the bubble tip; to do so, we exploit computational results obtained elsewhere[26] for the Bretherton problem in a tapered channel.

This paper is organized as follows. The model for the symmetric flow configuration of Fig. 1 is presented in Sec. II; the asymptotic theory is formulated in Sec. III, and a further approximation appropriate to peeling motion is described in Sec. IV; the asymptotic predictions are tested against existing simulation in Sec. V; asymptotics, new boundary-element results, and experimental data for the asymmetric flow configuration of Fig. 9 are compared in Sec. VI; and the results are discussed in Sec. VII. In three appendices we provide an interpretation of peeling as an integral force balance, some important regression formulas, and details of the asymptotics for the asymmetric flow.

II. STATEMENT OF THE FULL REOPENING PROBLEM

We treat here the model presented previously[13] and illustrated in Fig. 1. A channel is formed by two membranes held under large longitudinal tension η^* and supported by springs with spring constant Γ^*. Within the channel is fluid of viscosity μ^*; inertial and gravitational effects are assumed to be negligible. A semi-infinite bubble, held at constant pressure p_b^*, is blown into the channel and it advances along the channel's midline with steady speed U^* relative to the channel. The flow is assumed to be uniform in the spanwise direction, and symmetric about the channel's midline. The surface tension of the air–liquid interface is γ^*, assumed uniform. Far ahead of the bubble tip, the fluid-filled channel has width $2H^*$, the springs are unstressed and the fluid is at rest relative to the channel walls. Far behind the bubble tip, the springs are compressed and a uniform liquid film of thickness H^* sits on each of the channel walls; here too the liquid is at rest with respect to the channel walls.

To nondimensionalize the problem, lengths are scaled on H^*, pressures on γ^*/H^*, and velocities on U^*, following Ref. 13. This yields four dimensionless parameters,

$$\Gamma = \frac{\Gamma^* H^{*2}}{\gamma^*}, \quad \eta = \frac{\eta^*}{\gamma^*}, \quad \mathrm{Ca} = \frac{\mu^* U^*}{\gamma^*},$$

and

$$p_b = \frac{p_b^* H^*}{\gamma^*}.$$

For given wall properties (fixed Γ and η), the dimensionless bubble pressure p_b must be determined as a function of the capillary number Ca. In most experiments the dimensionless wall tension is large (e.g., $\eta > 240$ in Refs. 15–17) and Ca lies in the range $0 < \mathrm{Ca} < 10$.

In the frame of the moving bubble, we introduce Cartesian coordinates (x,y) with their origin at the bubble tip (Fig. 1), so that the upper wall of the channel lies along $y = h(x)$ and the air–liquid interface lies along $y = f(x)$ in $x \leqslant 0$, where $f(0) = 0$. The x axis lies along the midline of the channel. Within the region occupied by fluid, the velocity field $\mathbf{u} = (u,v)$, the stress tensor $\boldsymbol{\sigma}$, and the pressure p satisfy the Stokes equations

$$\nabla \cdot \mathbf{u} = 0, \tag{1a}$$

$$\nabla \cdot \boldsymbol{\sigma} = 0, \tag{1b}$$

$$\boldsymbol{\sigma} = -\mathrm{I}p + \mathrm{Ca}(\nabla \mathbf{u} + \nabla \mathbf{u}^T). \tag{1c}$$

Symmetry requires that $u_y = 0$ and $v = 0$ along $y = 0$ in $x > 0$.

The air–liquid interface $y = f$ is a streamline, is free of tangential stress, and the normal-stress jump is balanced by surface tension, so that here

$$\mathbf{u} \cdot \mathbf{n} = 0, \tag{2a}$$

$$\boldsymbol{\sigma} \cdot \mathbf{n} = -(\kappa + p_b)\mathbf{n}, \tag{2b}$$

where $\mathbf{n} = (f_x, -1)/(1 + f_x^2)^{1/2}$ is the unit normal along $y = f$ pointing out of the fluid and $\kappa = f_{xx}/(1 + f_x^2)^{3/2}$ is the interfacial curvature.

As in Ref. 13, the channel wall is assumed to be a membrane that moves normal to itself in the laboratory frame and tangential to itself in the moving frame, and the normal stress at the wall is balanced by the elastic forces due to the springs and wall tension. Thus, along $y = h(x)$, which has unit normal $\mathbf{m} = (-h_x, 1)/(1 + h_x^2)^{1/2}$, we have

$$\mathbf{u} = \frac{(-1, -h_x)}{(1 + h_x^2)}, \tag{3a}$$

$$-\mathbf{m} \cdot \boldsymbol{\sigma} \cdot \mathbf{m} = \Gamma \frac{(h-1)}{(1 + h_x^2)^{1/2}} - \eta \frac{h_{xx}}{(1 + h_x^2)^{3/2}}. \tag{3b}$$

It is assumed that the springs may slide freely in the x direction so that they always remain vertical. (Heil[14] has shown that the precise choice of wall model has only a modest qualitative effect on the overall behavior for this two-dimensional problem.) We restrict attention here to the limit in which the mean dimensionless wall tension η is large, assuming that small variations in wall tension arising from tangential viscous stresses may be neglected.[13] We therefore ignore the tangential-stress boundary condition along the membrane.

In the bubble-tip frame of reference, far ahead of the bubble (as $x \to \infty$), where the channel is collapsed,

$$\mathbf{u} \to (-1, 0), \quad \text{for} \quad 0 \leqslant y \leqslant h, \tag{4a}$$

$$h \to 1, \tag{4b}$$

and far behind the bubble (as $x \to -\infty$), where the channel is inflated,

$$\mathbf{u} \to (-1, 0), \quad \text{for} \quad f \leqslant y \leqslant h, \tag{5a}$$

$$h \to 1 + \frac{p_b}{\Gamma}, \tag{5b}$$

$$f \to \frac{p_b}{\Gamma}. \tag{5c}$$

In steady state, there is a uniform volume flux of fluid,

$$\int_f^h u \, dy = -1, \tag{6}$$

in the x direction throughout the entire flow domain (defining $f \equiv 0$ in $x > 0$ for convenience).

III. AN ASYMPTOTIC APPROXIMATION FOR LARGE WALL TENSION

We seek an asymptotic solution of (1)–(6) when the membrane tension is large, so that the membrane slope is uniformly small. To motivate the analysis, we first identify (in Sec. III A) the dominant scalings of the flow when the bubble advances with a peeling motion (as sketched in Fig. 2), i.e., when the springs are weak enough for the inflated section of the channel to be substantially wider than the fluid-filled-section. These scaling predictions are supported by a more formal analysis in Secs. III B–III F and IV.

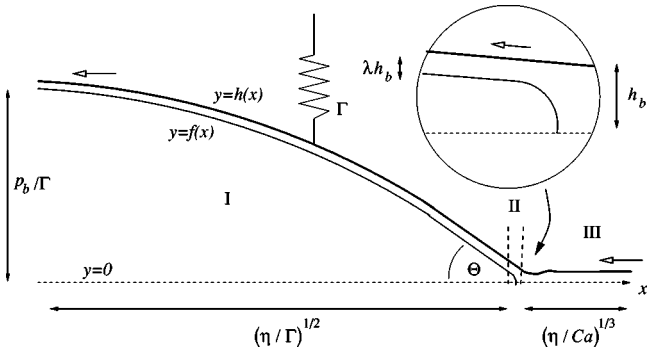

FIG. 3. The three asymptotic regimes, with the dominant length scales indicated. The inset shows how region II resembles the Bretherton problem.

A. Leading-order scalings for peeling motion

The asymptotic approximation is constructed by splitting the solution domain into the three regions illustrated in Fig. 3.

In region I, the channel is inflated by the bubble, and the fluid layer sits passively on the channel wall. Here the channel has approximate width $p_b/\Gamma \gg 1$ [from 5(b)], and its approximate length $(\eta/\Gamma)^{1/2} \gg 1$ is controlled by a balance of tension and spring forces [see 3(b)]. This implies that the peeling angle Θ near the bubble tip (see Fig. 3) is $O[p_b/(\eta\Gamma)^{1/2}]$. We expect Θ to be small when the membrane tension is large.

Region II, the neighborhood of the bubble tip, has $O(1)$ length and width, and here the flow is inherently two dimensional. However, since (by assumption) the local membrane slope is small ($\Theta \ll 1$), the leading-order flow in region II is equivalent to that of a bubble advancing into a parallel-sided channel, the so-called "Bretherton" problem.[18] It is well known from numerical and asymptotic studies of this problem[20,22–24,27,28] how the thickness of the film deposited behind the advancing bubble depends on the capillary number Ca. In effect, the flow here acts as a low-Reynolds number valve that determines the flow rate of the entire system. The small slope of the channel walls in this region does not affect the flow at leading order.

In region III, membrane tension, viscosity, and elastic forces determine the force required to pull the channel walls apart. We define the characteristic length of this region as $1/\epsilon$, where $\epsilon \ll 1$ may be determined as follows. If wall tension controls the pressure distribution (spring forces being relatively weak), then $\Gamma \ll \epsilon^2\eta$ [from (3b) with $h=O(1)$]. Then (3b) implies that the axial pressure gradient has magnitude $\epsilon^3\eta$. This balances viscous stresses of $O(\mathrm{Ca})$ [from 1(b) and 1(c)], implying that

$$\epsilon = (\mathrm{Ca}/\eta)^{1/3} \equiv (\mu^* U^*/\eta^*)^{1/3}. \tag{7}$$

This gives a second estimate of the peeling angle at the bubble tip, namely $\Theta = O[(\mathrm{Ca}/\eta)^{1/3}]$, and shows that the fluid pressure in this region is of magnitude $p_{\mathrm{III}} \sim \eta^{1/3}\mathrm{Ca}^{2/3}$.

Matching the two estimates of peeling angle Θ from regions I and III gives an initial estimate of the bubble pressure,

$$p_b \sim \Gamma^{1/2}\eta^{1/6}\mathrm{Ca}^{1/3}, \tag{8}$$

where here "$\sim$" means "scales like." Evidence supporting (8), which is valid when $\epsilon \ll 1$ and $\Gamma \ll \epsilon^2\eta$, i.e., for $(\Gamma^3/\eta)^{1/2} \ll \mathrm{Ca} \ll \eta$, is provided immediately by experimental observations.[15–17,29,30] In dimensional terms, (8) gives $p_b^* \sim \Gamma^{*1/2}\eta^{*1/6}(\mu^* U^*)^{1/3}$, which is independent of H^*, as seen in experiments;[15,17] this is associated with the peeling of membranes stuck together with vanishingly small fluid volumes. Further, if p_b^* is scaled with the width of the inflated channel ($D^* \sim p_b^*/\Gamma^*$) rather than H^*, then $p_b^*/(\gamma^*/D^*) \sim \eta^{1/3}\mathrm{Ca}^{2/3}$, which is independent of Γ^*, only weakly dependent on wall tension and an increasing function of Ca, again as observed experimentally.[16,17] More detailed quantitative comparisons with experiment will be made in Sec. VI below.

The condition of wall tension dominating spring stiffness in region III, $\Gamma \ll \epsilon^2\eta$, is equivalent to $\delta \ll 1$, where

$$\delta = \frac{p_b}{p_{\mathrm{III}}} = \left(\frac{\Gamma^3}{\eta\,\mathrm{Ca}^2}\right)^{1/6} \equiv \left(\frac{\Gamma^{*3}H^{*6}}{\eta^*\mu^{*2}U^{*2}}\right)^{1/6}. \tag{9}$$

Thus, in peeling motion, the fluid pressure p_{III} is substantially greater in magnitude than the bubble pressure. This is contrary to scaling arguments presented in Ref. 13, which took no account of matching peeling angles, but is supported by numerical results.[13,14] As we show below, it is the very low fluid pressure p_{III} that holds together the membranes, and that provides the dominant resistance to reopening. An alternative view of peeling motion in terms of an integral force balance is given in Appendix A, where it is shown that the total imposed axial force due to inflating the bubble is balanced entirely within region I.

In contrast, the limit $\delta \gg 1$ corresponds to "pushing motion" (Fig. 2), for which $\mathrm{Ca} \to 0$ and for which spring forces are dominant over membrane tension; this limit was treated in detail previously.[13]

B. Asymptotic analysis

We now proceed with a formal analysis, by deriving the leading-order problems in the three regions illustrated in Fig. 3 (in Secs. III C–III E), and then showing how the solutions in each region may be matched together (Sec. III F), yielding the nonlinear eigenvalue problem given in (22) and (33).

The full problem as stated in Sec. II has three independent parameters: Ca, η, and Γ. It is convenient to reformulate the problem in terms of ϵ, δ, and Ca [see (7) and (9)] before constructing matched asymptotic expansions, taking $\epsilon \ll 1$ as the perturbation parameter and assuming that δ and Ca are both $O(1)$. The special case in which $\epsilon \ll 1$ and $\delta \ll 1$, which gives the leading-order prediction (8), is treated in Sec. IV.

The limit $\epsilon \ll 1$ corresponds physically to the assumption that the membrane slope is uniformly small. We therefore assume that at leading order the channel width varies everywhere on a long $O(1/\epsilon)$ length scale, with small corrections arising in region II that vary over an $O(1)$ length scale. Thus we set

$$h(x) = H(X) + \epsilon^3\hat{h}(x), \tag{10a}$$

$$x = X/\epsilon. \tag{10b}$$

We assume that all flow variables depend on x in the inner region II, and on X in the outer regions I and III, so that $\hat{h}$ vanishes in regions I and III. We will match regions I and II by taking the limits $X\to 0-$ and $x\to -\infty$, and regions II and III via the limits $X\to 0+$ and $x\to\infty$. We have anticipated that the correction $\hat{h}$ in (10) is given by a balance in region II between viscous stresses, of $O(\mathrm{Ca})$, and membrane tension, of $O(\eta)$ [see (1) and (3b)], leading to h perturbations of magnitude $O(\mathrm{Ca}/\eta)=O(\epsilon^3)$.

We proceed by recasting the governing equations (1)–(6) in terms of ϵ, Ca, and δ, scaling the fluid pressure on p_{III} and the bubble pressure on the estimate (8), so that

$$p(x,y)=(\mathrm{Ca}/\epsilon)P(x,y), \tag{11a}$$

$$p_b=(\delta\mathrm{Ca}/\epsilon)P_b\,. \tag{11b}$$

Thus in the fluid, (1) and (6) become

$$\nabla\cdot\mathbf{u}=0, \tag{12a}$$

$$\mathbf{0}=-\nabla P+\epsilon\nabla^2\mathbf{u}, \tag{12b}$$

$$\int_f^{H+\epsilon^3\hat{h}} u\,dy=-1, \tag{12c}$$

with $u_y=v=0$ on $y=0$ for $x>0$. On $y=f$, in $x<0$, (2) becomes

$$\mathbf{u}\cdot\mathbf{n}=0, \tag{13a}$$

$$P-2\epsilon\mathbf{n}\cdot\mathbf{e}\cdot\mathbf{n}=(\epsilon/\mathrm{Ca})\kappa+\delta P_b\,, \tag{13b}$$

$$\mathbf{t}\cdot\mathbf{e}\cdot\mathbf{n}=0, \tag{13c}$$

where $\mathbf{n}$ and κ are as defined in Sec. II, $\mathbf{t}=(1,f_x)/(1+f_x^2)^{1/2}$ is the unit tangent, and $\mathbf{e}=\frac{1}{2}(\nabla\mathbf{u}+\nabla\mathbf{u}^T)$ is the rate-of-strain tensor. On $y=H(X)+\epsilon^3\hat{h}$, we have $\mathbf{m}=(-\epsilon H_X,1)/(1+\epsilon^2H_X^2)^{1/2}+O(\epsilon^4)$, and (3) becomes

$$\mathbf{u}=\frac{(-1,-\epsilon H_X)}{(1+\epsilon^2H_X^2)}+O(\epsilon^4), \tag{14a}$$

$$P-2\epsilon\mathbf{m}\cdot\mathbf{e}\cdot\mathbf{m}=\delta^2(H-1)-H_{XX}-\epsilon\hat{h}_{xx}+O(\epsilon^2), \tag{14b}$$

where the small terms on the right-hand-sides of (14a) and (14) involve H and $\hat{h}$ alone. The farfield conditions (4) and (5) imply

$$\mathbf{u}\to(-1,0),\quad H\to 1,\qquad (X\to\infty), \tag{15}$$

$$\mathbf{u}\to(-1,0),\quad H\to 1+(P_b/\delta),\quad f\to P_b/\delta,\quad (X\to-\infty). \tag{16}$$

C. Region I: The inflated channel

In the outer region in $X<0$, we set $P=P_0+\epsilon P_1+\epsilon^2P_2+O(\epsilon^3)$, $\mathbf{u}=\mathbf{u}_0+\epsilon\mathbf{u}_1+O(\epsilon^2)$, assuming all variables depend on X. Thus taking $f=f(X)$ implies that $\mathbf{n}=(\epsilon f_X,-1)+O(\epsilon^2)$ and $\kappa=O(\epsilon^2)$. At leading order, (10), (12), (14) in $X<0$ imply that $\nabla P_0=0$ with $P_0=\delta P_b$ and

$$\delta P_b=\delta^2(H-1)-H_{XX}\,, \tag{17}$$

with $H\to 1+(P_b/\delta)$ as $X\to-\infty$. Thus, in terms of $h_b\equiv H(0)$,

$$H(X)=\left(1+\frac{P_b}{\delta}\right)-\left(1+\frac{P_b}{\delta}-h_b\right)e^{\delta X}, \tag{18}$$

so that as $X\to 0-$,

$$H\sim h_b-\theta X+O(X^2), \tag{19a}$$

$$\theta\equiv P_b+\delta(1-h_b). \tag{19b}$$

All equations are satisfied up to the next two orders in ϵ by $\mathbf{u}=(-1,-\epsilon H_X)+O(\epsilon^2)$, $P_1=P_2=0$, $f=H-1$. Thus with error $O(\epsilon^2)$, the fluid sits passively on the membrane as a uniform film of unit thickness, and the membrane shape is controlled by a balance between wall tension and the springs.

D. Region III: The fluid-filled channel

In the outer region in $X>0$, we again assume all variables depend on X, which is equivalent to making a lubrication-theory approximation. The mass and momentum equations (12b) and (12c) become, with error $O(\epsilon^2)$,

$$0=-P_X+u_{yy}\,, \tag{20a}$$

$$0=-P_y\,, \tag{20b}$$

$$\int_0^H u\,dy=-1, \tag{20c}$$

with $u_y(X,0)=0$, $u(X,H)=-1+O(\epsilon^2)$, and

$$P(X,H)=\delta^2(H-1)-H_{XX}+O(\epsilon^2). \tag{21}$$

The velocity field is readily found to be $u=-1-\frac{1}{2}P_X(H^2-y^2)$, so the flux condition (20c) implies that, with error $O(\epsilon^2)$, $P_X=3(1-H)/H^3$. Thus, the wall shape is determined in $X>0$ by

$$\tfrac{1}{3}H^3(H_{XXX}-\delta^2H_X)=H-1, \tag{22a}$$

$$H\to 1\quad\text{as}\quad X\to\infty, \tag{22b}$$

which must be solved subject to suitable boundary conditions at the bubble tip, (i.e., as $X\to 0+$). Linearization about $H=1$ shows[13] that there is a two-parameter family of eigenmodes of (22) that decay in amplitude as $X\to\infty$, but that are oscillatory in X if $\delta<(243/4)^{1/6}$.

E. Region II: The bubble tip

Near the bubble tip, where $x=O(1)$, we set $P=\delta P_b+\epsilon\hat{P}(x,y)$, taking $\hat{P}$ and $\mathbf{u}(x,y)$ to be $O(1)$, so that (14b) at leading order gives (17), showing that the leading-order wall shape is governed by the same balance as in region I. From Sec. III A, we expect the wall slope to be continuous across region II, so that (19) implies

$$H\sim h_b-\epsilon\theta x+O(\epsilon^2), \tag{23}$$

throughout region II. Thus, locally the channel walls are flat but slightly tilted. Equations (12a)–(12c) become, up to $O(\epsilon^2)$,

$$\nabla\cdot\mathbf{u}=0, \tag{24a}$$

$$0=-\nabla\hat{P}+\nabla^2\mathbf{u}, \tag{24b}$$

$$\int_f^{h_b-\epsilon\theta x} u\,dy=-1, \tag{24c}$$

for $f\leqslant y\leqslant h_b-\epsilon\theta x$ (where $f\equiv 0$ in $x>0$), with $u_y=v=0$ on $y=0$ in $x>0$. On the bubble interface, (13) becomes

$$\mathbf{u}\cdot\mathbf{n}=0, \tag{25a}$$

$$\hat{P}-2\mathbf{n}\cdot\mathbf{e}\cdot\mathbf{n}=(\kappa/\mathrm{Ca}), \tag{25b}$$

$$\mathbf{t}\cdot\mathbf{e}\cdot\mathbf{n}=0, \tag{25c}$$

where κ and $\mathbf{n}$ are again as defined in Sec. II. On the channel wall, $y=h_b-\epsilon\theta x+O(\epsilon^2)$, (14) becomes

$$\mathbf{u}=(-1,-\epsilon\theta)+O(\epsilon^2), \tag{26a}$$

$$\hat{P}-2\mathbf{m}\cdot\mathbf{e}\cdot\mathbf{m}=-\hat{h}_{xx}+O(\epsilon), \tag{26b}$$

where $\mathbf{m}=(-\epsilon\theta,1)+O(\epsilon^2)$. The normal stress condition (26b) can be used to determine flow-induced perturbations to the uniform height, but these perturbations are weak [$O(\epsilon^3)$, as in (10)] and can henceforth be neglected.

The channel width at the bubble tip, h_b, can be scaled out of (24)–(26) under the transformation $\mathbf{x}=h_b\tilde{\mathbf{x}}$, $\hat{\mathbf{u}}=\hat{\mathbf{u}}$, $\mathbf{e}=\tilde{\mathbf{e}}/h_b$, $f=h_b\tilde{f}$, $h=h_b\tilde{h}$, $\kappa=\tilde{\kappa}/h_b$, and $\hat{P}=\hat{P}/h_b$. Then (24) becomes, with error $O(\epsilon^2)$,

$$\tilde{\nabla}\cdot\tilde{\mathbf{u}}=0, \tag{27a}$$

$$0=-\tilde{\nabla}\tilde{\mathbf{P}}+\tilde{\nabla}^2\tilde{\mathbf{u}}, \tag{27b}$$

$$\int_{\tilde{f}}^{1-\epsilon\theta\tilde{x}}\tilde{u}\,d\tilde{y}=-(1/h_b), \tag{27c}$$

for $\tilde{f}\leqslant\tilde{y}\leqslant 1-\epsilon\theta\tilde{x}$, subject to

$$\tilde{\mathbf{u}}\cdot\mathbf{n}=0, \tag{28a}$$

$$\tilde{P}-2\mathbf{n}\cdot\tilde{\mathbf{e}}\cdot\mathbf{n}=(\tilde{\kappa}/\mathrm{Ca}), \tag{28b}$$

$$\mathbf{t}\cdot\tilde{\mathbf{e}}\cdot\mathbf{n}=0, \tag{28c}$$

on the bubble interface and

$$\tilde{\mathbf{u}}=(-1,-\epsilon\theta), \quad \text{on} \quad \tilde{y}=1-\epsilon\theta\tilde{x}. \tag{29}$$

The flow governed by (27)–(29) is sketched in Fig. 4. It corresponds to a semi-infinite bubble advancing into a uniformly convergent channel. A uniform film of thickness $\lambda(\mathrm{Ca},\epsilon\theta)$ is deposited on the channel wall as $\tilde{x}\to-\infty$, where

$$\tilde{f}\to 1-\epsilon\theta\tilde{x}-\lambda, \tag{30a}$$

$$\tilde{\mathbf{u}}\to(-1,-\epsilon\theta). \tag{30b}$$

From (27c), we must have $\lambda=1/h_b$. Far ahead of the bubble tip, as $\tilde{x}\to\infty$, lubrication theory predicts a velocity profile $u=-1-\tilde{P}_{\tilde{x}}(\tilde{h}^2-\tilde{y}^2)$, where $\tilde{h}\equiv 1-\epsilon\theta\tilde{x}$. Since the flux here is also $-\lambda$, this requires that $\tilde{P}_{\tilde{x}}=3(\lambda-\tilde{h})/\tilde{h}^3$. Thus, the pressure distribution as $\tilde{x}\to\infty$ is

$$\tilde{P}\sim\int_0^{\tilde{x}}\frac{3}{\tilde{h}^3}(\lambda-\tilde{h})\,d\tilde{x}+\mathcal{P}, \tag{31}$$

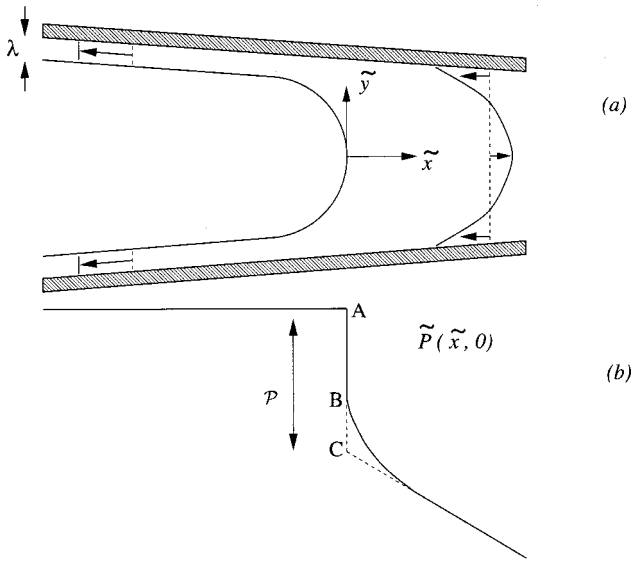

FIG. 4. The flow near the bubble tip in region II, showing (a) the bubble shape and velocity profiles, and (b) the pressure distribution along the channel midline. The pressure drop AB arises from surface tension acting at the bubble nose; the further drop BC arises largely from viscous normal stresses at the bubble tip. The total drop AC is represented by $\mathcal{P}<0$ (after Ref. 21).

for some $\mathcal{P}(\mathrm{Ca},\epsilon\theta)<0$, which represents the pressure jump across region II arising from viscous and capillary forces,[6,18,20,21] as illustrated in Fig. 4(b).

Taking the limit $\epsilon\theta\to 0$, the problem (27)–(31) reduces to the planar Bretherton problem, i.e., a semi-infinite bubble entering a parallel-sided channel of unit width. The quantities $\lambda_0(\mathrm{Ca})=\lambda(\mathrm{Ca},0)$, $\mathcal{P}_0(\mathrm{Ca})=\mathcal{P}(\mathrm{Ca},0)$ have been computed numerically by numerous authors over a wide range of capillary numbers; both quantities are plotted in Fig. 5. For $\mathrm{Ca}\to 0$, $\lambda_0(\mathrm{Ca})\sim 1.337\,\mathrm{Ca}^{2/3}$ and $\mathrm{Ca}\,\mathcal{P}_0(\mathrm{Ca})\sim -1.0-3.80\,\mathrm{Ca}^{2/3}$ (see Refs. 6, 18, 24). Regression formulas for λ_0 and $\mathcal{P}_0$, taken from numerical studies[20,22–24] are given in (B1) and (B2).

Both $\lambda(\mathrm{Ca},\epsilon\theta)$ and $\mathcal{P}(\mathrm{Ca},\epsilon\theta)$ have recently been computed[26] for a bubble advancing into a convergent channel over a wide range of taper angles $\epsilon\theta$ and capillary numbers Ca. For our purposes it is sufficient to know only the leading-order effects of taper on the deposited film thickness, which is expressed as the quantity λ_1 in the expansion

$$\lambda(\mathrm{Ca},\epsilon\theta)=\lambda_0(\mathrm{Ca})+\epsilon\theta\lambda_1(\mathrm{Ca})+O(\epsilon^2), \tag{32a}$$

$$\mathcal{P}(\mathrm{Ca},\epsilon\theta)=\mathcal{P}_0(\mathrm{Ca})+O(\epsilon). \tag{32b}$$

Here $\lambda_1(\mathrm{Ca})$ is plotted in Fig. 5(a) and a regression formula is given in (B3a); note that λ_1 and λ_0 have the same asymptote as $\mathrm{Ca}\to 0$. For $0<\mathrm{Ca}\lesssim 10.74$, very weak taper increases slightly the thickness of the deposited film. However, for larger values of Ca, or for larger taper angles [represented by neglected terms in (32a)], the deposited film thickness can be significantly reduced by channel taper.[26]

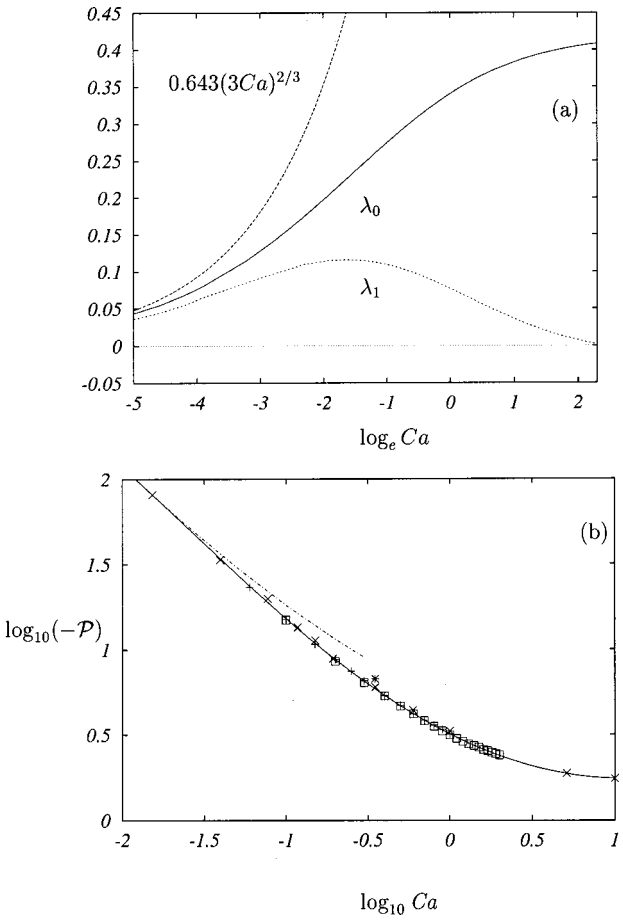

FIG. 5. (a) λ_0(Ca) and λ_1(Ca) (from Ref. 26) plotted alongside their low-Ca asymptote; (b) numerical data (×, Ref. 20; +, Ref. 23; squares, Ref. 24) are replotted, with a nonlinear curve fit [solid line (B2)]. The single point marked with * is taken from Fig. 3 of Ref. 22. The dashed line shows the asymptotic small-Ca limit Ca $\mathcal{P}\sim -1-3.8\,\mathrm{Ca}^{2/3}$.

F. Matching

To match regions I and II, we rewrite the outer limit of region II (30) in terms of outer variables, so that with error $O(\epsilon^2)$, $f\sim h_b-\theta X-h_b\lambda$ and $\mathbf{u}_0\sim(-1,-\epsilon\theta)$ as $x\to-\infty$. As we have seen already, $h_b\lambda=1$, ensuring a match with the limit $X\to 0-$ in Sec. III C. Thus, with error $O(\epsilon^2)$, continuity of mass demands that

$$H(0)=1/\lambda. \tag{33a}$$

The slope of the membrane θ [see (19)] must be continuous across region II, so that, with error $O(\epsilon^2)$, it is

$$H_X(0)=-P_b+\delta\left(\frac{1}{\lambda}-1\right). \tag{33b}$$

The curvature of the membrane jumps across region II because of a rapid variation of pressure. We match regions II and III to determine a condition on $H_{XX}(0+)$, which, with (33a) and (33b), will provide boundary conditions for (22) as $X\to 0+$. The pressure in region II as $x\to\infty$, given (31) is, in terms of outer variables,

$$P\sim\delta P_b+\int_0^X\frac{3}{H^3}(1-H)\,\mathrm{d}X+\frac{\epsilon\mathcal{P}}{h_b},$$

so as $X\to 0+$ we have, with error $O(\epsilon^2)$, using (21),

$$H_{XX}(0)=\delta^2\left(\frac{1}{\lambda}-1\right)-\epsilon\mathcal{P}_0\lambda_0-\delta P_b. \tag{33c}$$

Finally, in (33a)–(33c) the quantity λ, to $O(\epsilon^2)$, satisfies (32a), i.e.,

$$\lambda=\lambda_0+\epsilon\left[P_b+\delta\left(1-\frac{1}{\lambda_0}\right)\right]\lambda_1. \tag{33d}$$

Equation (22) has a two-parameter family of solutions. The three boundary conditions in (33) can only be satisfied for certain values of P_b. This is therefore a nonlinear eigenvalue problem for P_b, dependent on the three parameters (ϵ, δ, Ca), accurate up to $O(\epsilon)$ in the limit $\epsilon\to 0$, with δ and Ca both $O(1)$. This problem can be solved numerically using finite differences and Newton's method; results are presented in Sec. V. First, however, we show how the dependence on parameters, and the structure of the solution, simplifies substantially in the limit $\delta\ll 1$.

IV. REOPENING AS A PEELING MOTION

The eigenvalue problem (22), (33) was derived assuming that membrane slopes are uniformly small ($\epsilon\ll 1$), but allowing the spring parameter δ to be $O(1)$. We now make the further, quite realistic, assumption that the springs are weak so that the bubble inflates to a width much greater than the thickness of the undisturbed fluid layer far ahead of the bubble, which corresponds to taking $\delta\ll 1$ (Sec. III A). In this case, (22), (33) can be simplified by expanding as follows:

$$H\sim H_0(X)+\delta H_1(X)+\epsilon H_2(X)+\cdots, \tag{34a}$$

$$P_b\sim P_{b0}+\delta P_{b1}+\epsilon P_{b2}+\cdots. \tag{34b}$$

For (34) to be strictly asymptotic, we require $\epsilon^2\ll\delta\ll 1$, and so for convenience we assume that $\epsilon\sim\delta\ll 1$. We show here how the scaling for peeling motion given in (8) is justified, yielding the refined asymptotic prediction (46).

A. The leading-order problem

The leading-order problem to be solved is [from (22)]

$$\tfrac{1}{3}H_0^3H_{0XXX}=H_0-1, \tag{35a}$$

$$H_0\to 1 \quad \text{as} \quad X\to\infty, \tag{35b}$$

subject to [from (33)]

$$H_0(0)=1/\lambda_0, \tag{36a}$$

$$H_{0X}(0)=-P_{b0}, \tag{36b}$$

$$H_{0XX}(0)=0. \tag{36c}$$

For $X\to\infty$, solutions of the Landau–Levich[31] equation (35) may be written as

$$H_0\sim 1+\alpha\exp[-\tfrac{1}{2}3^{1/3}(X-X_0)]\cos[\tfrac{1}{2}3^{1/3}\sqrt{3}(X-X_0)], \tag{37}$$

for constants α and X_0. This function repeats itself if X increases by $4\pi/(3^{1/3}\sqrt{3})$ and α increases by a factor $\exp[2\pi/\sqrt{3}]$.[19] By fixing X_0, say, and varying α, one can

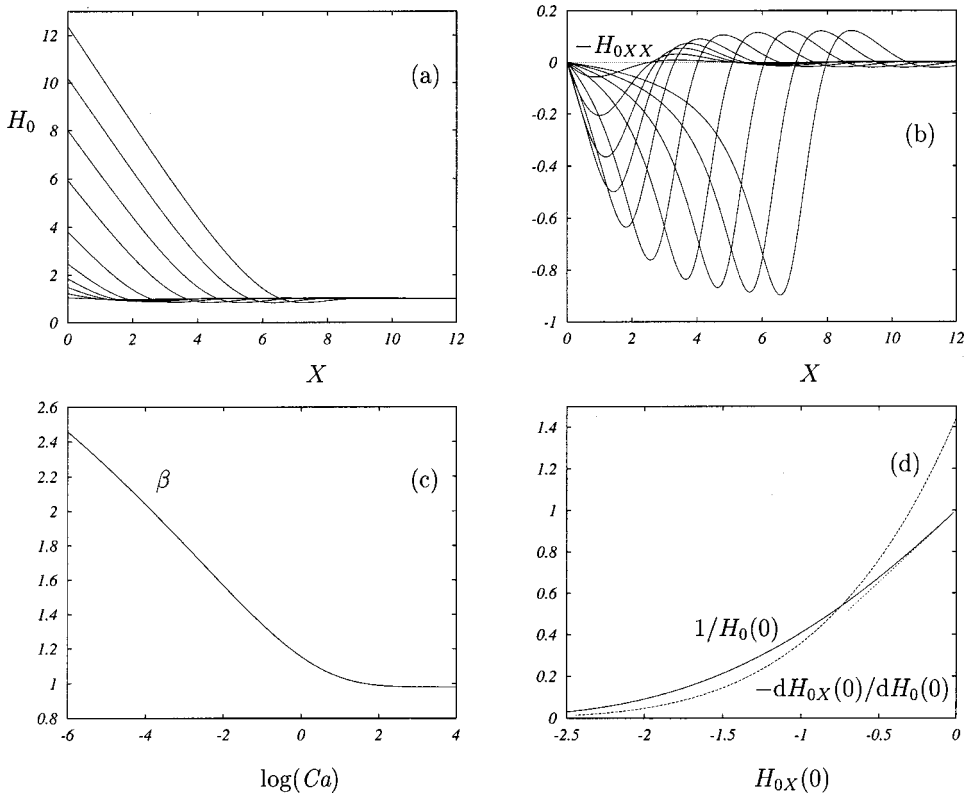

FIG. 6. (a) Solutions of (35) for which $H_{0XX}(0)=0$: (b) shows the corresponding values of $-H_{0XX}(X)$ (proportional to the pressure); (c) $\beta(\mathrm{Ca})=-H_{0X}(0)$ plotted against log Ca; (d) $1/H_0(0)$ (solid) and $-dH_{0X}(0)/dH_0(0)$ (dotted) plotted versus the peeling angle $H_{0X}(0)$. The straight dashed line in (d) shows $1+H_{0X}(0)/3^{1/3}$, obtained from (37).

shoot with X decreasing until $H_{0XX}=0$ at some point, which may then be shifted to the origin. It is thereby straightforward to construct the one-parameter family of solutions of (35) for which $H_{0XX}(0)=0$; these are shown in Figs. 6(a) and 6(b). The correspondence between $H_0(0)$ and $H_{0X}(0)$ is shown in Fig. 6(d). Note that the minimum film thickness in $X>0$ is never much smaller than 1 [Fig. 6(a)], although the pressure minimum may be large [Fig. 6(b)].

To solve (35), (36) for a given Ca, we find λ_0 using (B1), $H_0(0)$ using (36a), and hence determine the scaled peeling angle $-H_{0X}(0)=\beta(\mathrm{Ca})$, say. Equation (36b) then gives a leading-order expression for the bubble pressure:

$$P_{b0}=\beta(\mathrm{Ca}). \tag{38}$$

Here β is plotted as a function of the capillary number in Fig. 6(c), and a regression formula for β is given in (B3b) below; β provides the $O(1)$ coefficient in (8) that could not be determined by scaling alone.

B. First-order corrections

To obtain the $O(\epsilon)$ and $O(\delta)$ corrections to (8), we return to the expansion (34) of (22), (33), which yields two linear problems:

$$H_{iXXX}=3H_iH_0^{-4}(3-2H_0), \tag{39a}$$

$$H_i(X\to\infty)\to 0 \quad (i=1,2), \tag{39b}$$

subject to

$$H_1(0)=0, \quad H_2(0)=-P_{b0}\lambda_1/\lambda_0^2, \tag{40a}$$

$$H_{1X}(0)=-\left(P_{b1}+1-\frac{1}{\lambda_0}\right), \quad H_{2X}(0)=-P_{b2}, \tag{40b}$$

$$H_{1XX}(0)=-P_{b0}, \quad H_{2XX}(0)=-\mathcal{P}_0\lambda_0. \tag{40c}$$

We proceed by noting that the elastic term in (22) does not arise at this order, so we need only consider solutions of (35). Typical solutions are shown in Fig. 6(a). Extended into $X<0$, these constitute all possible solutions of (35); they form a two-parameter family, parametrized by a downstream amplitude (α) and a translation in X (X_0), as indicated by (37). Since, for fixed Ca, we are linearizing about a particular solution $H_0(X;X_0,\alpha_0)$, we seek a solution of (39) in the form

$$H\sim H_0+H_i+\cdots\equiv H_0(X;X_0,\alpha_0)+[\,\delta X H_{0X}(X;X_0,\alpha_0)+\delta\alpha H_{0\alpha}(X;X_0,\alpha_0)]+\cdots,$$

for $i=1,2$, where, for $\delta X\ll 1$, $\delta\alpha\ll 1$, from (36),

$$H_0(0;X_0,\alpha_0)=1/\lambda_0(\mathrm{Ca}), \tag{41a}$$

$$H_{0X}(0;X_0,\alpha_0)=-\beta(\mathrm{Ca}), \tag{41b}$$

$$H_{0XX}(0;X_0,\alpha_0)=0. \tag{41c}$$

We may then write

$$\delta X H_{0X}(0;X_0,\alpha_0)+\delta\alpha H_{0\alpha}(0;X_0,\alpha_0)=H_i(0), \tag{42a}$$

$$\delta X H_{0XX}(0;X_0,\alpha_0)+\delta\alpha H_{0X\alpha}(0;X_0,\alpha_0)=H_{iX}(0), \tag{42b}$$

$$\delta X H_{0XXX}(0;X_0,\alpha_0)+\delta\alpha H_{0XX\alpha}(0;X_0,\alpha_0)=H_{iXX}(0). \tag{42c}$$

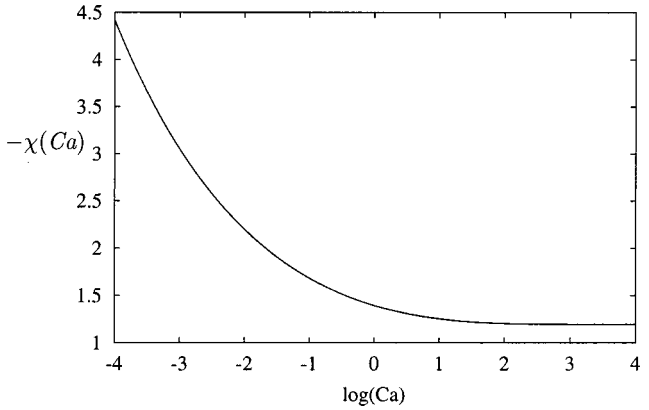

FIG. 7. The function χ(Ca [(44) solid], and the regression formula [(B3c) dashed].

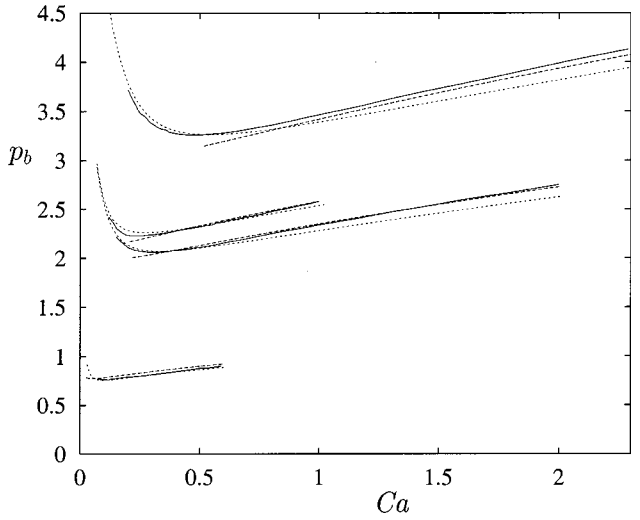

FIG. 8. Computational results (solid) from Fig. 14 of Ref. 13 are compared with asymptotic predictions obtained using the formula (46) (dashed) and numerically using (22), (33) (dotted) for, from top to bottom, $(\Gamma,\eta)=(1, 100)$, (0.5, 250), (0.5, 100), (0.1, 100); when Ca=1, $(\delta,\epsilon)\approx$ (0.46, 0.22), (0.28, 0.16), (0.33, 0.22), (0.15, 0.22), respectively.

Given (41) and the fact that $H_{0X\alpha}(0;X_0,\alpha)/H_{0\alpha}(0;X_0,\alpha) = \mathrm{d}H_{0X}(0)/\mathrm{d}H_0(0)$ [a function plotted in Fig. 6(d)], we obtain from (35), (41), (42),

$$H_{iX}(0)=\frac{\mathrm{d}H_{0X}(0)}{\mathrm{d}H_0(0)}\left(H_i(0)+\frac{\beta H_{iXX}(0)}{3(\lambda_0^2-\lambda_0^3)}\right). \tag{43}$$

Thus, defining

$$\chi(\mathrm{Ca})=\frac{\beta}{3(\lambda^2-\lambda^3)}\frac{\mathrm{d}H_{0X}(0)}{\mathrm{d}H_0(0)} \tag{44}$$

(see Fig. 7), a regression formula for which is given in (B3c), we can use (40), (43) to give

$$P_{b1}=\chi\beta+\lambda_0^{-1}-1, \quad P_{b2}=\chi[\mathcal{P}_0\lambda_0+3(1-\lambda_0)\lambda_1].$$

Thus (34b) becomes

$$P_b\sim\beta+\delta[\lambda_0^{-1}-1+\chi\beta]+\epsilon\chi[\lambda_0\mathcal{P}_0+3(1-\lambda_0)\lambda_1], \quad \text{as} \quad \epsilon\to 0, \quad \delta\to 0, \tag{45}$$

where λ_0, $\mathcal{P}_0$, λ_1, β and χ are given approximately by (B1)–(B3). The initial prediction (8) may therefore be refined as follows:

$$p_b\approx\beta\Gamma^{1/2}\eta^{1/6}\mathrm{Ca}^{1/3}+\Gamma[\lambda_0^{-1}-1+\chi\beta] +\Gamma^{1/2}\eta^{-1/6}\mathrm{Ca}^{2/3}\chi[\lambda_0\mathcal{P}_0+3(1-\lambda_0)\lambda_1]. \tag{46}$$

Equations (45), (46) are valid for $\epsilon^2\ll\delta\ll 1$, and the dominant error is $O(\epsilon^2)$.

V. COMPARISON WITH EXISTING NUMERICAL SIMULATIONS

The asymptotic prediction (45), including the $O(\epsilon)$ and $O(\delta)$ corrections, when written in terms of the original variables in (46), shows clearly how there are three distinct contributions to the bubble pressure when the wall tension is large ($\epsilon\ll 1$) and the springs are weak ($\delta\ll 1$). The dominant contribution ($P_b\sim\beta$) comes from the viscous peeling forces in region III. The two further contributions are an $O(\delta)$ correction due to the presence of the springs, and an $O(\epsilon)$ correction due partly to the viscous capillary pressure drop across the bubble tip [region II, Fig. 4(b)], and partly to the effects of channel taper near the bubble tip. This prediction approximates solutions of the full nonlinear eigenvalue problem (22), (33).

Figure 8 shows a comparison between (46), numerical solutions of (22), (33), and computational simulations of the reopening problem.[13] There is excellent quantitative agreement between (22), (33) and the simulations near the turning point on each curve. The asymptotic predictions underestimate p_b slightly as Ca increases, which is because the small-slope parameter ϵ increases with Ca (ϵ rises toward 0.3 at the right-hand end of the uppermost curve). Large values of η are required for $\epsilon=(\mathrm{Ca}/\eta)^{1/3}$ to be small, and so for the parameter values used here inclusion of the $O(\epsilon)$ terms in (22), (33) makes a substantial difference to the accuracy of the asymptotic predictions. The explicit prediction (46) agrees well with both other datasets on the right-hand branch of each curve, but fails to capture the turning point accurately because δ is not small along the left-hand solution branch. The small difference between (46) and (22), (33) for larger Ca arises because the former represents an expansion of the latter in ϵ and δ; the fact that (46) lies closer to the simulations is therefore fortuitous.

VI. COMPARISON WITH EXPERIMENT

We now turn to a quantitative comparison of the theoretical model with the experiments of Perun and Gaver,[16] who explored the reopening problem using Newtonian lining fluid in a planar geometry in which one membrane was bound to a plane surface and the other was confined by a layer of foam that acted like a set of linear springs (Fig. 9). Let H^* now be the thickness of the channel when undisturbed, and let lengths be scaled on H^*, pressures on γ^*/H^*, and velocities on U^*. The primary difference between the resulting problem and that described in Sec. II (for the symmetric configuration on Fig. 1) is that the no-slip condition must be applied along $y=0$ instead of a symmetry

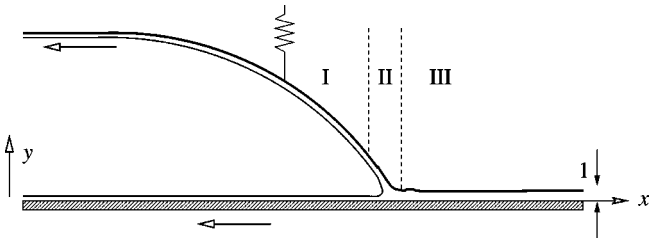

FIG. 9. The configuration used in Ref. 16: one membrane is fixed to a plane wall, the other is supported by linear springs and is held under longitudinal tension. Asymptotic regions I–III are indicated.

condition. In what follows, we assume that the liquid layer separates symmetrically between the flexible membrane and the rigid wall, so that the film thicknesses on the rigid wall and on the membrane as $x \to -\infty$ are both $\frac{1}{2}$.

Modest adaptions to the asymptotic analysis, appropriate to this new geometry, are described in Appendix C. We also conducted new boundary-element simulations with experimental parameter values, using techniques outlined in Sec. VI A. Direct comparisons between computation, asymptotics, and experimental data are presented in Sec. VI B.

A. Boundary-element calculations

Computational simulations of the steady-state reopening of the asymmetric system shown in Fig. 9 follow the methods described in Ref. 13. Within the computational domain, which includes the bubble tip (region II) and extends into regions I and III to either side, the Stokes equations (1) are solved using a boundary-element method subject to kinematic and interfacial stress conditions (2) at the air–liquid interface and (3) at the flexible membrane. Along the rigid wall $y=0$, $\mathbf{u}=(-1,0)$. End conditions for the computational domain are provided by upstream and downstream regions (within regions I and III), where the lubrication approximation is assumed to hold. For example, in region I, the pressure gradient within the liquid layer along the membrane is given by

$$\frac{1}{2} = \frac{H^3}{3\,\mathrm{Ca}}\, p_x + H,$$

where H is the thickness of the deposited film; likewise (C1) describes the pressure gradient in region III.

To identify a steady-state solution, an initial domain shape is assumed. For a specified Ca, the bubble pressure, meniscus, and wall positions are iterated sequentially using Newton's method so as to simultaneously satisfy (2a) along the interface and the wall stress condition (3b) at the flexible membrane. Iterations are continued until (2b), (3a) are met to a specified tolerance.

Figure 10 shows examples of the membrane and bubble shape for increasing Ca obtained numerically, demonstrating how the region of channel that is inflated ahead of the bubble tip diminishes as Ca increases, while the membrane slope at the bubble tip rises sharply. The corresponding stresses on the membrane are shown in Fig. 11. Both normal and tangential stresses grow rapidly in magnitude as Ca increases,

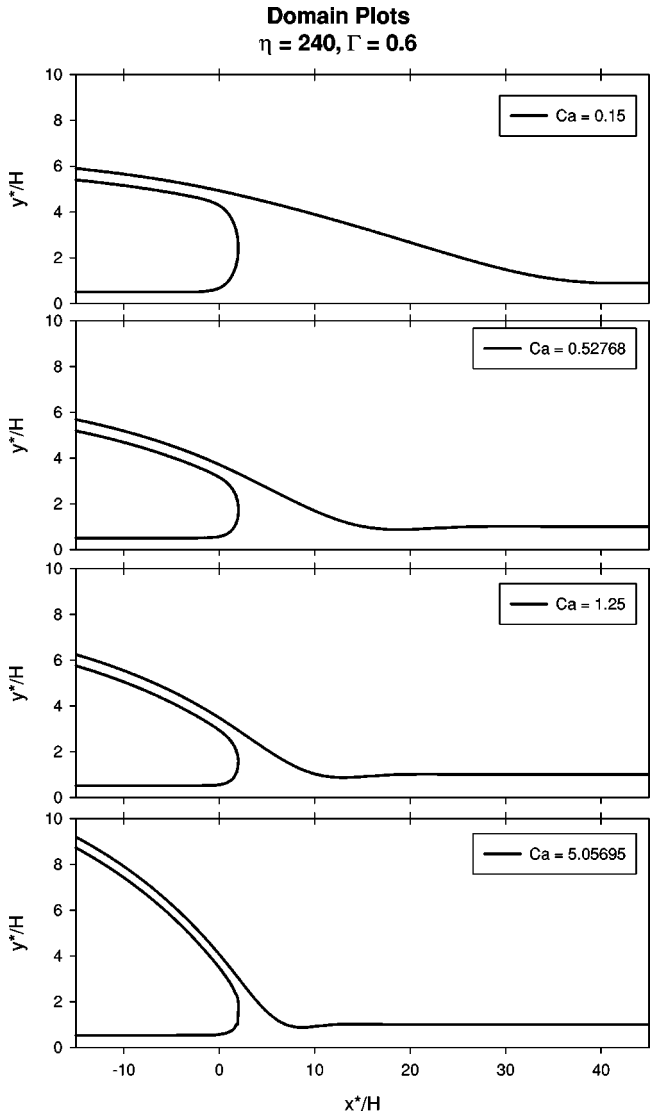

FIG. 10. Membrane and bubble shapes for Ca=0.15, 0.527 68, 1.25, and 5.056 95, with $\Gamma=0.6$ and $\eta=240$, obtained using the boundary-element method.

although the large inward normal stress ahead of the bubble tip is significantly greater in magnitude than any tangential stress.

B. Direct comparison

The $p_b - \mathrm{Ca}$ relation obtained by simulation is compared with experimental data[16] in Fig. 12. Despite numerous approximations in the theoretical model, the full simulation shows good agreement with experiment over a wide range of Ca. The simulation predicts a turning point in the $p_b - \mathrm{Ca}$ curve near $\mathrm{Ca} \approx 0.15$, $p_b \approx 3.46$ for these parameter values, well below the lowest values of Ca investigated in the experiments. The computations slightly underestimate experimental results at large Ca; this may arise partly through inertial effects, which can lead to elevated reopening pressures, even at moderate Reynolds numbers.[14]

Also shown in Fig. 12 is the corresponding asymptotic prediction computed using (22), (C6), valid for $\epsilon \ll 1$, $\delta = O(1)$, and the prediction (C7), valid for $\epsilon^2 \ll \delta \ll 1$. The

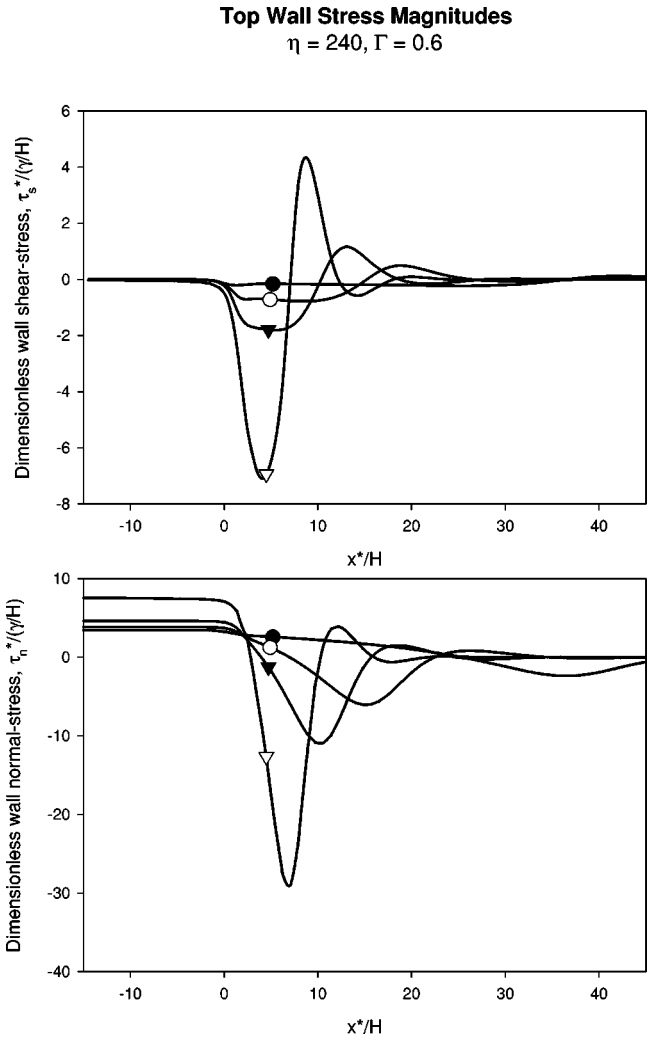

FIG. 11. Dimensionless wall shear stress (top) and wall normal stress (bottom) for Ca=0.15 (solid circle), 0.527 68 (open circle), 1.25 (solid triangle), and 5.056 95 (open triangle), as functions of x, for $\Gamma=0.6$ and $\eta=240$, corresponding to Fig. 10.

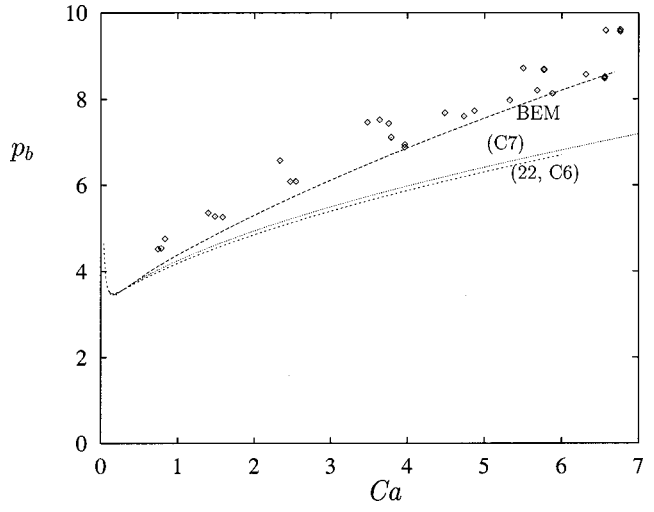

FIG. 12. A comparison with data from Fig. 9 of Ref. 16 (symbols), $\eta=240$, $\Gamma=0.6$, with boundary element simulations (BEM, long dashes), and the asymptotic approximations [(22), (C6)] (short dashes) and (C7) (dotted).

former agrees well with computational results for $\mathrm{Ca}\ll 1$, predicting a turning point in the $p_b-\mathrm{Ca}$ curve near $\mathrm{Ca}\approx 0.16$, $p_b\approx 3.49$. Immediately beyond the turning point (C7) also agrees well with the simulation. However, both asymptotic predictions diverge from the simulation and experiment as Ca increases further, because the small-slope parameter ϵ rises sharply beyond $\mathrm{Ca}\approx 1$: for example, $\epsilon\approx 0.3$ when $\mathrm{Ca}\approx 1.6$ and $\epsilon\approx 0.4$ when $\mathrm{Ca}\approx 3.85$. Nevertheless, the correct qualitative behavior is captured even when the membrane slope is quite large.

VII. DISCUSSION

Using new boundary-element simulations, we have demonstrated that a theoretical model representing the steady motion of a semi-infinite bubble in a flexible-walled channel can accurately reproduce experimental observations over a wide range of capillary numbers (Fig. 12). We have also developed a rational asymptotic approximation for this model that agrees closely with both experiment and simulation over a substantial range of Ca, for bubble motion in both a symmetric (Fig. 8) and an asymmetric channel (Fig. 12).

The asymptotic approximation involves two parameters, ϵ and δ, defined in (7), (9). The limit $\epsilon\ll 1$ corresponds to large membrane tension and small membrane slope. When $\epsilon\ll 1$, $\delta=O(1)$, the asymptotic analysis requires solution of a third-order nonlinear eigenvalue problem (22), (33), (C6). The resulting predictions capture accurately the turning point in the curve relating bubble pressure p_b to bubble speed Ca (e.g., Figs. 8 and 12), all of the left-hand solution branch and a significant fraction of the right-hand solution branch. The asymptotic analysis simplifies further when $\delta\ll 1$, where δ corresponds to the ratio of the thickness of the undisturbed fluid layer between the membranes far ahead of the bubble to the inflated bubble width; in this case the motion at the bubble tip is essentially a peeling motion. A double expansion in powers of ϵ and δ leads to an explicit prediction for p_b (46), (C7) obtained from solutions of the Landau–Levich equation (35). The resulting predictions accurately capture that part of the right-hand solution branch for which membrane slopes are uniformly small.

The asymptotic prediction diverges from computational simulation as Ca increases, since for larger bubble speeds the peeling angle increases and ϵ is no longer small. The asymptotic model, which retains all the $O(1)$ and $O(\epsilon)$ terms in an expansion of p_b in powers of ϵ, includes the first-order effects of channel taper near the bubble tip through the function $\lambda_1(\mathrm{Ca})$. However, a recent numerical study of bubble motion in a uniformly convergent channel[26] has shown that the effects of strong taper have significant and unexpected effects that are not captured by λ_1. Whereas for small taper angles the film thickness deposited behind an advancing bubble increases slightly with channel slope [since $\lambda_1>0$ in (32a) for $0<\mathrm{Ca}\lesssim 10.74$; see Fig. 5(a)], at large Ca the film thickness falls substantially as the taper angle increases. This finite-slope effect, if included in our model, would bring the asymptotic prediction closer to the computations. While the effects of the other finite-slope corrections have not been investigated, this observation suggests

that channel taper near the bubble tip has a significant influence on bubble pressures in rapid peeling motion.

The asymptotic model can be readily adapted to other geometries and flow conditions. The regression formulas presented in Appendix B enable simple predictions to be made of a wide class of peeling motions, for example. The asymptotic model has recently been extended to incorporate unsteady effects,[32] to verify the expected stability properties of the two solution branches in Fig. 2 and to reproduce the transient pressure fluctuations during the initiation of airway reopening that have been observed experimentally.[15,16] The asymptotic analysis may also be useful for future investigations of the fingering and elastic instabilities that have been observed experimentally in this problem[15,17,29] and in closely related problems involving peeling[19] and roll coating.[33–35] The slight tilt of the walls in the neighborhood of the interface has a slight stabilizing influence on potential fingering instabilities,[33] but roll-coating computations,[20,36] relating the critical capillary numbers above which a planar meniscus becomes unstable to the local peeling angle, suggest that the experiments are all in a strongly supercritical (i.e., unstable) regime. However, the close agreement between two-dimensional (2D) computations and experiment (Fig. 12) suggests that fingering instabilities may not have a significant effect on reopening pressures.

In peeling motion, with $(\Gamma^3/\eta)^{1/2} \ll \mathrm{Ca} \ll \eta$, the asymptotic analysis gives a leading-order relationship between the speed of advance of the bubble and the dynamic peeling angle (denoted Θ in Fig. 3) in the form

$$\Theta = (A\,\mathrm{Ca}/\eta)^{1/3}\beta(\mathrm{Ca}), \quad A = \begin{cases} 1, & \text{if } u_y(x,0) = 0, \\ 4, & \text{if } u(x,0) = -1, \end{cases} \tag{47}$$

where β is given by (B3b) [see also Fig. 6(d)]. With its $\mathrm{Ca}^{1/3}$ scaling, (47) is reminiscent of Tanner's law relating the apparent contact angle to the speed of an advancing contact line.[1,37] The value of the factor A depends on the experimental configuration, i.e., whether the line $y=0$ is a line of symmetry or a rigid boundary (Fig. 9); in the latter case the parameter A contains the usual factor of 4 that arises in lubrication theory when the pressure-gradient-driven flux between a no-slip and a stress-free boundary is compared with the flux between two no-slip boundaries. By computing a quasistatic wall shape in region I, assuming $h=0$ and $h_x = -\theta$ at the bubble tip, a leading-order prediction for p_b follows immediately from (47).

The scalings identified in Sec. III A here have direct physiological implications. In peeling motion, we have shown that an advancing bubble of pressure p_b^* that inflates a model airway from a collapsed, fluid-filled thickness H^* to an inflated (dimensional) diameter D^*, advances with speed U^*, where

$$p_b^* \sim \eta^{*1/3}\mu^{*2/3}U^{*2/3}/D^*, \tag{48}$$

where $(\sim)$ here represents the leading-order scaling relationship in the limit $(\Gamma^3/\eta)^{1/2} \ll \mathrm{Ca} \ll \eta$. This pressure is relatively insensitive to H^* and surface tension γ^*, although γ^* contributes at leading order to the yield pressure for steady bubble propagation, which scales like γ^*/D^*;[17] γ^* also contributes to corrections to (48) such as those given in (46), which can be significant for practical parameter values. As demonstrated in Fig. 11, the greatest stresses exerted on the airway walls are low (adhesive) fluid pressures, of magnitude $p_b^* D^*/H^* \gg p_b^*$, which extend a distance $H^*(\eta^*/\mu^* U^*)^{1/3} \sim H^* \eta^{*1/2}/(p_b^* D^*)^{1/2}$ ahead of the bubble. Thus, an individual epithelial cell in an initially fluid-filled airway will experience a suction of magnitude $p_b^* D^*/H^*$ over a time scale $H^* \mu^* \eta^*/(p_b^* D^*)^2$ as a bubble approaches it, and then sustained compression of magnitude p_b^* once the bubble has passed. Airways are therefore potentially subject to harmful overinflation if p_b^* is too large, and to possibly even more severe damage due to transient but very low extensional normal stresses. Tracheal epithelial cells are known to exhibit a biological response to sustained compressive stresses;[38] it is not clear how epithelial cells respond either to suction or to very abrupt pressure changes. It is obviously also important to establish to what extent these planar results apply to the significantly more complex three-dimensional geometry of a collapsed, buckled, lung airway. Fully three-dimensional models of this problem are at an early but promising stage.[39,40]

The asymptotic analysis demonstrates clearly how the steady-state bubble pressure is sensitive at leading order to the thickness of the film deposited behind the bubble tip [through the parameter β; Fig. 6(c)]. For systems that are not "clean," but for which the surface tension varies due to the presence of surfactants, a thickening of the deposited film (the typical effect of surfactants, at least at low capillary numbers[41,42]) would require the channel to be narrower at the bubble tip, the peeling angle to be smaller [Fig. 6(a)], and the bubble pressure to be lower. A reduction in the mean surface tension at the bubble tip would also be equivalent to reducing the peeling angle and bubble pressure [since β falls with Ca; Fig. 6(d)]. The increased pressure drop across the bubble tip due to the increased viscous stresses associated with an immobilized interface [associated with the quantity $\mathcal{P}$; see Fig. 4(b)], is a second-order effect in peeling motion according to this analysis. These estimates are consistent with the predictions of a recent numerical study of surfactant effects on airway reopening under bulk equilibrium conditions.[43] However, due to the great range of physical and chemical properties of surfactants, large regions of parameter space await investigation.

ACKNOWLEDGMENTS

D.P.G. would like to acknowledge the support of the National Institute of Health (NIH) through Grant No. HL51334, the National Science Foundation (NSF) through Grants No. BCS-9358207 and No. DMF-9709754, and the Department of Energy (DOE) through the Livingston Digital Millenium Center for Computational Science at Tulane and Xavier Universities (DE-FG-02-01ER633196). D.H. was supported by EPSRC Grant No. GR/M84572.

APPENDIX A: AN INTEGRAL FORCE BALANCE FOR PEELNG MOTION

Integrating $\nabla\cdot\boldsymbol{\sigma}$ [see (1)] across a control volume bounded by $y=0$, $y=h$ and the lines $x=\pm L$, where $L\gg 1$ (in the configuration shown in Fig. 3), applying the divergence theorem and taking the x component of the resulting forces yields[13]

$$-1+p_bD+\int_{\substack{y=h\\-L\leqslant x\leqslant L}}\hat{\mathbf{x}}\cdot\boldsymbol{\sigma}\cdot\mathbf{n}\,\mathrm{d}s=0,\quad\text{where}\quad D=1+\frac{p_b}{\Gamma},\tag{A1}$$

where $\hat{\mathbf{x}}=(1,0)$. The first term in (A1) comes from surface tension acting along the bubble interface, and p_bD represents the applied force on the left of the domain; s is the arc length along the membrane measured in the x direction, and along $y=0$ there is no force in the x direction because it is a line of symmetry. For a peeling motion for which $D\approx p_b/\Gamma\gg 1$, we may approximate the integral by evaluating the leading-order terms across regions I, II, and III separately, so that (A1) becomes

$$\frac{p_b^2}{\Gamma}+\int_{\substack{\mathrm{I}\\D\geqslant y\geqslant 0}}p_b\,\mathrm{d}y+\int_{\substack{\mathrm{III}\\O\leqslant x<\infty}}[h_xp+\mathrm{Ca}\,u_y(x,h)]\,\mathrm{d}x=O(1,\mathrm{Ca}).\tag{A2}$$

Each term on the left-hand side of (A2) is $O(\eta^{1/3}\,\mathrm{Ca}^{2/3})$. The shear stress on the membrane in region II gives rise to a smaller contribution of $O(\mathrm{Ca})$. Since the membrane slope is small we have used lubrication theory to give the leading-order terms in region III: h_xp represents the x component of the pressure force per unit length acting on the nonhorizontal membrane in region III, and $\mathrm{Ca}\,u_y(x,h)$ the x component of the viscous shear stress acting on the membrane. Now lubrication theory also implies that

$$u=-\frac{p_x}{2\,\mathrm{Ca}}(h^2-y^2)-1,\tag{A3}$$

in region III (a result equivalent to this is given in Sec. III D). Thus, $\mathrm{Ca}\,u_y=hp_x$ on $y=h$, so the region III integral in (A2) becomes $[hp]_0^\infty$. Now for peeling motion $\delta\ll 1$, or equivalently $p_b\ll p_{\mathrm{III}}$, so that to leading order in ϵ and δ we must take $p=0$ at both ends of region III [the equivalent upstream limit is given in 36(c)]. Thus, the integrated pressure and shear-stress forces in region III cancel and the dominant balance in (A2) is between the imposed pressure force p_bD and the x component of the pressure force acting on the inflated membrane in region I.

APPENDIX B: REGRESSION FORMULAS

Halpern and Gaver[22] give the following regression formula for λ_0:

$$\lambda_0(\mathrm{Ca})\approx\lambda_{0\,\mathrm{app}}(\mathrm{Ca})=0.417(1-\exp[-1.69\,\mathrm{Ca}^{0.5025}]).\tag{B1}$$

While this formula is inaccurate at very small Ca, it agrees with the numerically computed λ_0 shown in Fig. 5(a) to within 3% for $\mathrm{Ca}>0.1$, the range of Ca of interest here. McEwan and Taylor[19] used a similar function based on experimental measurements in their semiempirical analysis. The pressure difference $\mathcal{P}_0(\mathrm{Ca})$ has been computed by a handful of authors.[20,23,24] Their data, and the single data point available from Ref. 22, are plotted in Fig. 5(b). The formula,

$$\log_{10}(-\mathcal{P}_{0\,\mathrm{app}})=-2.008\,58+8.924\,26\times\exp[-0.038\,332(Z+5)^{2.173\,98}]+0.898\,217Z,\tag{B2}$$

where $Z\equiv\log_{10}\mathrm{Ca}$, provides an acceptable approximation to $\mathcal{P}_0(\mathrm{Ca})$ for $10^{-2}\leqslant\mathrm{Ca}\leqslant 10$. A simpler approximation for $\mathcal{P}_0$ was also used in Ref. 44.

The following formulas:

$$\lambda_{1\,\mathrm{app}}=0.0769-0.041\,19z-4.63\times10^{-3}z^2+4.46\times10^{-3}z^3+2.474\,42\times10^{-4}z^4-2.129\,54\times10^{-4}z^5-2.512\,64\times10^{-5}z^6,\tag{B3a}$$

$$\beta_{\mathrm{app}}(\mathrm{Ca})=0.988\,113+(0.366\,815-0.184\,297z)\times\exp(-0.000\,159\,689(z+8)^{4.085\,38}),\tag{B3b}$$

$$-\chi_{\mathrm{app}}(\mathrm{Ca})=-0.234\,261+1.630\,71\exp(-0.3487z)+0.368\,093z-0.027\,983\,2z^2,\tag{B3c}$$

where $z\equiv\log\mathrm{Ca}$, are graphically indistinguishable from, respectively, λ_1 in Fig. 5(a) for $-5\leqslant z<2$, β in Fig. 6(c) for $|z|<4$; and χ [see (44)] in Fig. 7 for $|z|<4$. The large number of significant figures used here ensures the regression error is uniformly small across the stated range of validity.

APPENDIX C: ASYMPTOTIC ANALYSIS FOR ASYMMETRIC REOPENING

The configuration used in Ref. 16, shown in Fig. 9, requires a modification to the analysis described in Secs. II–IV. In region III, for example, the no-slip condition along $y=0$ demands that, in terms of the original dimensionless variables, the lubrication theory approximation for the flux becomes

$$-1=-\frac{p_xh^3}{12\,\mathrm{Ca}}-h,\tag{C1a}$$

$$p=\Gamma(h-1)-\eta h_{xx}.\tag{C1b}$$

The only difference between this and the former case is that the original factor $3\,\mathrm{Ca}$ becomes a factor $12\,\mathrm{Ca}$. We therefore reformulate the problem using

$$\tilde{\epsilon}\equiv\left(\frac{4\,\mathrm{Ca}}{\eta}\right)^{1/3},\tag{C2a}$$

$$\hat{\delta}=\frac{\Gamma^{1/2}}{\hat{\epsilon}\,\eta^{1/2}},\tag{C2b}$$

$$x=\frac{\hat{X}}{\hat{\epsilon}}, \tag{C2c}$$

$$p=\eta\hat{\epsilon}^2 P, \tag{C2d}$$

$$p_b=\hat{\delta}\eta\hat{\epsilon}^2 P_b, \tag{C2e}$$

where Γ is now defined with respect to the total channel width ahead of the bubble. The leading-order problem (C1) is then exactly (22), with δ replaced by $\hat{\delta}$ and X by $\hat{X}$.

Since region I is quasistatic, this change has no leading-order effect, and the peeling angle is still given by (19b), although the dimensionless film thickness has value $\frac{1}{2}$ along the membrane.

In region II (assuming the bubble advances so that films of equal thickness are deposited on each wall), we again follow the procedure described in Sec. III E, but now variables are scaled slightly differently. We first set $P=\hat{\delta}P_b+(\hat{\epsilon}/4)\hat{P}$, recovering (24a) (24b), (25), and (26a), with ϵ replaced by $\hat{\epsilon}$. We then introduce new coordinates $(\tilde{x},\tilde{y})$, with (0,0) located at the bubble tip and the $\tilde{x}$ axis aligned with the line of symmetry between $y=0$ and $y=h_b-\hat{\epsilon}\theta x$; the $\tilde{x}$ axis therefore makes an angle $\frac{1}{2}\hat{\epsilon}\theta$ to the x axis. Rescaling by the local channel half-width $\frac{1}{2}h_b$, setting

$$\tfrac{1}{2}h_b\tilde{x}=x-\tfrac{1}{2}\hat{\epsilon}\theta(y-\tfrac{1}{2}h_b), \tag{C3}$$

$$\tfrac{1}{2}h_b\tilde{y}=\tfrac{1}{2}\hat{\epsilon}\theta x+(y-\tfrac{1}{2}h_b), \tag{C4}$$

and $\kappa=2\tilde{\kappa}/h_b$, $\hat{P}=2\tilde{P}/h_b$, etc., we then recover (27a), (27b), and (28). Instead of (29), we have $\mathbf{u}=(-1,-\hat{\epsilon}\theta)$ on $\tilde{y}=1-\frac{1}{2}\hat{\epsilon}\theta\tilde{x}$, with error $O(\hat{\epsilon}^2)$. Since there is unit total flux through region II, we again have $\lambda h_b=1$, and the pressure where regions II and III overlap becomes

$$P\sim\tilde{\delta}P_b+\int_0^{\hat{X}}\frac{3}{H^3}(1-H)\mathrm{d}\hat{X}+\frac{\hat{\epsilon}}{2}\mathcal{P}\lambda, \tag{C5}$$

where $\lambda=\lambda(\mathrm{Ca},\frac{1}{2}\hat{\epsilon}\theta)$ and $\mathcal{P}=\mathcal{P}(\mathrm{Ca},\frac{1}{2}\hat{\epsilon}\theta)$. The matching conditions then give the following boundary conditions for region III:

$$H(0)=1/\lambda, \tag{C6a}$$

$$H_{\hat{X}}(0)=-P_b+\hat{\delta}\left(\frac{1}{\lambda}-1\right), \tag{C6b}$$

$$H_{\hat{X}\hat{X}}(0)=\hat{\delta}^2\left(\frac{1}{\lambda}-1\right)-\hat{\delta}P_b-\tfrac{1}{2}\hat{\epsilon}\mathcal{P}_0\lambda_0, \tag{C6c}$$

$$\lambda=\lambda_0+\tfrac{1}{2}\hat{\epsilon}\left[P_b+\hat{\delta}\left(1-\frac{1}{\lambda_0}\right)\right]\lambda_1. \tag{C6d}$$

Again these conditions are very similar to (33); the primary differences are the factors of $\frac{1}{2}$ in (C6c) and (C6d). We can then expand in powers of $\hat{\epsilon}$ and $\hat{\delta}$, as in Sec. IV, to obtain [cf. (45)]

$$P_b\sim\beta+\hat{\delta}(\lambda_0^{-1}-1+\chi\beta)+\tfrac{1}{2}\hat{\epsilon}\chi[\lambda_0\mathcal{P}_0+3(1-\lambda_0)\lambda_1],$$
$$\hat{\epsilon}\ll 1,\quad \hat{\delta}\ll 1. \tag{C7}$$

[1] L. Leger and J. F. Joanny, "Liquid spreading," Rep. Prog. Phys. **55**, 431 (1992).
[2] A. Oron, S. H. Davis, and S. G. Bankoff, "Long-scale evolution of thin liquid films," Rev. Mod. Phys. **69**, 931 (1997).
[3] G. F. Teletzke, H. T. Davis, and L. E. Scriven, "How liquids spread on solids," Chem. Eng. Commun. **55**, 41 (1987).
[4] R. Burridge and J. B. Keller, "Peeling, slipping and cracking—some one-dimensional free-boundary problems in mechanics," SIAM Rev. **20**, 31 (1978).
[5] D. A. Spence and P. Sharpe, "Self-similar solutions for elastohydrodynamic cavity flow," Proc. R. Soc. London **400**, 289 (1985).
[6] C. W. Park and G. M. Homsy, "Two-phase displacement in Hele–Shaw cells: Theory," J. Fluid Mech. **139**, 291 (1984).
[7] P. G. Saffman and G. I. Taylor, "The penetration of a fluid into a porous medium or Hele–Shaw cell containing a more viscous liquid," Proc. R. Soc. London **245**, 312 (1958).
[8] P. T. Macklem, D. F. Proctor, and J. C. Hogg, "The stability of peripheral airways," Respir. Physiol. **8**, 191 (1970).
[9] J. B. Grotberg, "Pulmonary flow and transport phenomena," Annu. Rev. Fluid Mech. **26**, 529 (1994).
[10] H. L. Halliday, "Surfactant replacement therapy," Pediatr. Pulmonol Suppl. **11**, 96 (1995).
[11] R. G. Brower, M. A. Matthay, A. Morris *et al.*, "Ventilation with lower tidal volumes as compared with traditional tidal volumes for acute lung injury and the acute respiratory distress syndrome," New England J. Med. **342**, 1301 (2000).
[12] J. G. Muscedere, J. B. M. Mullen, K. Gan, and A. S. Slutsky, "Tidal ventilation at low airway pressures can augment lung injury," Am. J. Respir. Crit. Care Med. **149**, 1327 (1994).
[13] D. P. Gaver III, D. Halpern, O. E. Jensen, and J. B. Grotberg, "The steady motion of a semi-infinite bubble through a flexible-walled channel," J. Fluid Mech. **319**, 25 (1996).
[14] M. Heil, "Finite Reynolds number effects in the propagation of an air finger into a liquid-filled flexible-walled channel," J. Fluid Mech. **424**, 21 (2000).
[15] M. L. Perun and D. P. Gaver III, "An experimental model investigation of the opening of a collapsed untethered pulmonary airway," ASME J. Biomech. Eng. **117**, 245 (1995).
[16] M. L. Perun and D. P. Gaver III, "Interaction between airway lining fluid forces and parenchymal tethering during pulmonary airway reopening," J. Appl. Physiol. **79**, 1717 (1995).
[17] D. P. Gaver III, R. W. Samsel, and J. Solway, "Effects of surface tension and viscosity on airway reopening," J. Appl. Physiol. **69**, 74 (1990).
[18] F. P. Bretherton, "The motion of long bubbles in tubes," J. Fluid Mech. **10**, 166 (1961).
[19] A. D. McEwan and G. I. Taylor, "The peeling of a flexible strip attached by a viscous adhesive," J. Fluid Mech. **26**, 1 (1966).
[20] K. J. Ruschak, "Boundary-conditions at a liquid–air interface in lubrication flows," J. Fluid Mech. **119**, 107 (1982).
[21] G. I. Taylor, "Cavitation of a viscous fluid in narrow passages," J. Fluid Mech. **16**, 595 (1963).
[22] D. Halpern and D. P. Gaver III, "Boundary-element analysis of the time-dependent motion of a semi-infinite bubble in a channel," J. Comput. Phys. **115**, 366 (1994).
[23] D. A. Reinelt, "Interface conditions for two-phase displacement in Hele–Shaw cells," J. Fluid Mech. **183**, 219 (1987).
[24] D. A. Reinelt and P. G. Saffman, "The penetration of a finger into a viscous fluid in a channel and tube," SIAM J. Sci. Stat. Comput. **6**, 542 (1985).
[25] D. J. Coyle, C. W. Macosko, and L. E. Scriven, "Film-splitting flows in forward roll coating," J. Fluid Mech. **171**, 183 (1986).
[26] D. Halpern and O. E. Jensen, "A semi-infinite bubble advancing into a planar tapered channel," Phys. Fluids **14**, 431 (2002).
[27] M. D. Giavedoni and F. A. Saita, "The axisymmetric and plane cases of a gas phase steadily displacing a Newtonian liquid—a simultaneous solution of the governing equations," Phys. Fluids **9**, 2420 (1997).
[28] D. B. Ingham, J. A. Ritchie, and C. M. Taylor, "The motion of a semi-infinite bubble between parallel plates," Z. Angew. Math. Phys. **43**, 191 (1992).
[29] S.-H. Hsu, K. P. Strohl, and A. M. Jamieson, "Role of viscoelasticity in tube model of airway reopening. I. Non-Newtonian sols," J. Appl. Physiol. **76**, 2841 (1994).
[30] H. T. Low, Y. T. Chew, and C. W. Zhou, "Pulmonary airway reopening:

Effects of non-Newtonian fluid viscosity,'' ASME J. Biomech. Eng. **119**, 298 (1997).
[31]L. D. Landau and B. Levich, ''Dragging of a liquid by a moving plate,'' Acta Physicochim. URSS **17**, 42 (1942).
[32]M. K. Horsburgh, Ph.D. thesis, University of Cambridge, 2000.
[33]J. R. A. Pearson, ''The instability of uniform viscous flow under rollers and spreaders,'' J. Fluid Mech. **7**, 481 (1960).
[34]E. Pitts and J. Greiller, ''The flow of thin liquid films between rollers,'' J. Fluid Mech. **11**, 33 (1961).
[35]K. J. Ruschak, ''Coating flows,'' Annu. Rev. Fluid Mech. **17**, 65 (1985).
[36]D. J. Coyle, C. W. Macosko, and L. E. Scriven, ''Stability of symmetric film-splitting between center-rotating cylinders,'' J. Fluid Mech. **216**, 437 (1990).
[37]L. H. Tanner, ''The spreading of silicone oil drops on horizontal surfaces,'' J. Phys. D **12**, 1473 (1979).
[38]B. Ressler, R. T. Lee, S. H. Randell, J. M. Drazen, and R. D. Kamm, ''Molecular responses of rat tracheal epithelial cells to transmembrane pressure,'' Am. J. Physiol. Lung Cell. Mol. Physiol. **278**, L1264 (2000).
[39]M. Heil, ''Minimal liquid bridges in non-axisymmetrically buckled elastic tubes,'' J. Fluid Mech. **380**, 309 (1999).
[40]M. Heil, ''Airway closure: occluding liquid bridges in strongly buckled elastic tubes,'' ASME J. Biomech. Eng. **121**, 487 (1999).
[41]J. Ratulowski and H.-C. Chang, ''Marangoni effects of trace impurities on the motion of long gas bubbles in capillaries,'' J. Fluid Mech. **210**, 303 (1990).
[42]K. J. Stebe and D. Barthès-Biesel, ''Marangoni effects of adsorption-desorption controlled surfactants on the leading end of an infinitely long bubble in a capillary,'' J. Fluid Mech. **286**, 25 (1995).
[43]D. Y. K. Yap and D. P. Gaver III, ''The influence of surfactant on two-phase flow in a flexible-walled channel under bulk equilibrium conditions,'' Phys. Fluids **10**, 1846 (1998).
[44]T. Maxworthy, ''Experimental study of interface instability in a Hele–Shaw cell,'' Phys. Rev. A **39**, 5863 (1989).